PROTEINS
STRUCTURE ■ FUNCTION ■ BIOINFORMATICS

Predicting order of conformational changes during protein conformational transitions using an interpolated elastic network model

Mustafa Tekpinar and Wenjun Zheng*

Department of Physics, University at Buffalo, Buffalo, New York 14260

ABSTRACT

The decryption of sequence of structural events during protein conformational transitions is essential to a detailed understanding of molecular functions of various biological nanomachines. Coarse-grained models have proven useful by allowing highly efficient simulations of protein conformational dynamics. By combining two coarse-grained elastic network models constructed based on the beginning and end conformations of a transition, we have developed an interpolated elastic network model to generate a transition pathway between the two protein conformations. For validation, we have predicted the order of local and global conformational changes during key ATP-driven transitions in three important biological nanomachines (myosin, F_1 ATPase and chaperonin GroEL). We have found that the local conformational change associated with the closing of active site precedes the global conformational change leading to mechanical motions. Our finding is in good agreement with the distribution of intermediate experimental structures, and it supports the importance of local motions at active site to drive or gate various conformational transitions underlying the workings of a diverse range of biological nanomachines.

Proteins 2010; 78:2469–2481.

Key words: conformational transition; elastic network model; transition pathway; myosin; F1 ATPase; chaperonin GroEL; power-stroke mechanism.

INTRODUCTION

Protein conformational dynamics[1,2] is critically involved in many biomolecular functions ranging from enzymatic catalysis[3–5] to allosteric regulation.[6–11] Protein dynamics spans a wide range of temporal scales (from femtoseconds to seconds) and spatial scales (from atomic fluctuations to collective domain motions). Among various protein functions, the workings of a number of biological nanomachines (including widely-studied molecular motors like myosin,[12] F_1 ATPase,[13] and chaperonin GroEL[14]) are thought to rely on highly coordinated conformational transitions between a series of biochemical states, some of which have been captured by X-ray crystal structures. However, it remains extremely challenging to experimentally probe or computationally model the transient intermediates of these key transitions, which hold keys to the dynamic mechanism of these fascinating nanomachines.

In complement with experimental efforts for probing protein dynamics at atomic resolution (such as NMR[15,16] and time-resolved X-ray crystallography[17]), structure-based computer modeling promises to elucidate the fine details of protein conformational changes. Given multiple crystal structures of a protein at different functional states, structural analysis is widely used to identify dynamic domains undergoing rigid-body motions,[18–20] and the residues involved in local conformational changes between these states.[21–24] To assist the visualization of conformational transitions between two crystal structures, several morphing techniques[25,26] have been developed to generate movies of chemically feasible conformations, although the biological relevance of these interpolated transition pathways remain uncertain. To obtain detailed dynamic information from static protein structures, atomistic molecular dynamics (MD)[27] and related methods (such as targeted MD[28] and biased MD[29]) have been employed to probe protein conformational fluctuations and transitions. Nevertheless, the atomistic MD simulations of protein dynamics are limited to a time-scale range of nanoseconds ~ microseconds[30] despite fast advancing computing technology.

To overcome the time-scale barrier for MD simulations, a variety of coarse-grained models[31,32] have been developed to simulate protein conformational dynamics with greater efficiency. For example, the Go model,[33] constructed based on the native residue contacts of a folded protein, has been successfully used to simulate conformational transitions between known

Additional Supporting Information may be found in the online version of this article.
Grant sponsor: American Heart Association; Grant number: 0835292N.
*Correspondence to: Wenjun Zheng, Department of Physics, University at Buffalo, Buffalo, New York 14260. E-mail: wjzheng@buffalo.edu.
Received 12 January 2010; Revised 31 March 2010; Accepted 7 April 2010
Published online 20 April 2010 in Wiley InterScience (www.interscience.wiley.com). DOI: 10.1002/prot.22755

protein structures.[34] Of particular interest to the present study is the elastic network model (ENM),[35–37] which represents a protein structure as a network of C_α atoms with neighboring ones connected by springs with a uniform force constant.[38] The normal mode analysis (NMA) of ENM often yields a handful of low-frequency modes that dominate the large-scale conformational changes observed between two protein crystal structures.[37,39,40] Numerous studies have established ENM as an efficient and robust means to tease out the functionally relevant conformational dynamics from protein structures with no limit in time scale or system size (for reviews, see Refs. 41–43). Indeed, ENM has formed the basis of several computational methods for modeling protein conformational transitions.[44–47] In an earlier study,[46] we proposed the mixed-ENM technique to sample conformational space using a double-well potential,[45–47,48] which is built from two ENM potentials constructed based on the beginning and end conformations of a transition. A similar approach (plastic network model) was proposed by Maragakis and Karplus.[45] In another related study by Delarue and coworkers, a transition path was generated by minimizing an ENM-based action function.[47] Although the applications of these techniques have produced biologically interesting results,[44–49] systematic validation remains to be done. In an effort toward this goal, Weiss and Levitt performed an evaluation of several coarse-grained morphing techniques by assessing how closely the modeled transition pathways approach intermediate crystal structures of five proteins.[50]

In this study, we will generalize the mixed-ENM formulation[46] by proposing a coarse-grained transition pathway modeling method named interpolated-ENM (iENM). The key idea of iENM is to solve the saddle points of a general double-well potential function constructed from two ENM potential functions based at the beginning and end conformations of a transition. This mathematical problem is converted to the search for the minima of a linear interpolation of the above two ENM potential functions (see "Methods" section). Besides its generality, the iENM aims to improve the accuracy of mixed-ENM method.[46] The mixed-ENM method uses the second order expansion of an ENM potential to enable an algebraic solution to the saddle point equation.[46] However, the accuracy of such expansion decreases significantly as we sample conformations further away from the minimal-energy structure. Therefore, the mixed-ENM method is not suitable for modeling large conformational changes. In this work, we will remedy this inaccuracy by exactly solving the saddle point equation (see Methods) to generate a pathway between the beginning and end conformations of a transition. The new protocol is highly efficient thanks to the use of a sparse linear equation solver in place of a more expensive eigen-solver (see Methods). In addition, the mixed-ENM method takes no account of residue-residue interactions absent from the beginning or end conformation of a transition.[46] So it is prone to residue-residue collisions, especially when the conformation change is large. To reduce residue-residue collisions, we will include a new steric energy term in addition to the elastic energy of ENM.

For validation, we will apply iENM to the ATP-driven conformational transitions in three biological nanomachines (myosin,[12] F_1 ATPase,[13] and GroEL[14]). We will critically assess the iENM-predicted transition pathways by evaluating how well they predict the order of local and global conformational changes in these tiny motors. In all three cases, iENM predicts that the local conformational change at the ATP-binding site precedes the global conformational change leading to large mechanical movement. This prediction is in good agreement with the order of structural events deduced from the intermediate crystal structures of these proteins. Our finding supports the importance of local motions at active site to drive or gate various conformational transitions underlying the workings of a diverse range of biological nanomachines.

METHODS

Elastic network model (ENM)

In an ENM, a protein structure is represented as a network of C_α atoms whose minimal-energy (or equilibrium) conformation is given by a crystal structure. A harmonic potential accounts for the elastic interaction between two C_α atoms that lie within a cutoff distance R_c (set to 10 Å[46]). The potential energy function of ENM is[38]

$$E_{\mathrm{ENM}} = \frac{1}{2}\sum_{i=2}^{N}\sum_{j=1}^{i-1} C_{ij}\theta(R_c - d_{ij}^0)(d_{ij} - d_{ij}^0)^2, \qquad (1)$$

where d_{ij} is the distance between the C_α atoms i and j, d_{ij}^0 is the value of d_{ij} as given in a crystal structure, N is the number of C_α atoms, and $\theta(x)$ is the Heaviside function. C_{ij} is the force constant of the spring between the C_α atoms i and j. C_{ij} is set to 10 for chemically bonded residues[51] ($j = i \pm 1$), and 1 otherwise (the unit of C_{ij} can be arbitrarily chosen without changing the modeling results).

The ENM potential energy can be expanded near a given conformation X_* to the second order:

$$E_{\mathrm{ENM}}(X) \approx E_{\mathrm{ENM}}(X_*) + \delta X^T G_* + \frac{1}{2}\delta X^T H_* \delta X, \qquad (2)$$

where $\delta X = X - X_*$, $G_* = \bigtriangledown E_{\mathrm{ENM}}|_{X=X_*}$ is the gradient of E_{ENM} at $X = X_*$, and H_* is a $3N \times 3N$ Hessian matrix given by

$$H_* = \sum_{i=2}^{N}\sum_{j=1}^{i-1} C_{ij}\theta(R_c - d_{ij}^0)H^{ij}, \qquad (3)$$

where the elements of the $3N \times 3N$ matrix H^{ij} are given by

$$H^{ij}_{\alpha_{i'},\beta_{j'}} = \frac{1}{2}\frac{\partial^2}{\partial\alpha_{i'}\partial_{\beta_{j'}}}\left[(d_{ij}-d^0_{ij})^2\right]\Big|_{X=X_*}, \quad (4)$$

where $\alpha_{i'} = x_{i'}, y_{i'}, z_{i'}$, ($\beta_{j'} = x_{j'}, y_{j'}, z_{j'}$) is the x, y, z component of the Cartesian coordinates of the C_α atom i' (j'). Note that the matrix elements of H^{ij} are nonzero only if ($i' = i$ and $j' = j$), or ($i' = j$ and $j' = i$), or ($i' = i$ and $j' = i$), or ($i' = j$ and $j' = j$).

Transition pathway modeled by iENM

We consider an arbitrary double-well potential function $F(E_1,E_2)$ with two minima at the beginning and end conformations of a transition. It satisfies: $F(E_1,E_2) \approx E_1$ if $E_1 \ll E_2$, and $F(E_1,E_2) \approx E_2$ if $E_2 \ll E_1$, where E_1 and E_2 are two single-well potentials. Remarkably, the transition pathways generated by iENM (see later) are independent of the mathematic form of $F(E_1,E_2)$ which varied in previous studies.[45,46,52] The saddle points (SP) of $F(E_1,E_2)$ are solved as follows:

$$0 = \nabla F(E_1,E_2) = \frac{\partial F}{\partial E_1}\nabla E_1 + \frac{\partial F}{\partial E_2}\nabla E_2, \quad (5)$$

which is equivalent to solving the following equation (after setting $\lambda = \frac{\partial F}{\partial E_1}\Big/\left(\frac{\partial F}{\partial E_1}+\frac{\partial F}{\partial E_2}\right)$)

$$0 = \lambda\nabla E_1 + (1-\lambda)\nabla E_2, \quad (6)$$

where λ is a parameter of interpolation that varies from 1 to 0 (assuming $\frac{\partial F}{\partial E_1} \geq 0$ and $\frac{\partial F}{\partial E_2} \geq 0$). Therefore, the problem of solving SP for the double-well potential function $F(E_1,E_2)$ is converted to the problem of finding the minima of a linearly interpolated potential function $\lambda E_1 + (1-\lambda)E_2$. Alternatively, Eq. (6) gives a set of minimal-energy crossing points between E_1 and E_2 where $E_1 = E_2$ is at minimum.

Based on the above general formulation, we propose an iENM protocol based on a double-well potential $F(E_{ENM1} + E_{col}, E_{ENM2} + E_{col})$, where E_{ENM1} and E_{ENM2} are two ENM potential functions [see Eq. (1)] based at the beginning and end conformations of a transition, and E_{col} is a steric collision energy defined as follows:

$$E_{col} = \frac{1}{2}\sum_{i=3}^{N}\sum_{j=1}^{i-2} C_{col}\theta(R_{col}-d_{ij})(d_{ij}-R_{col})^2, \quad (7)$$

where $R_{col} = 4$ Å, $C_{col} = 10$, and chemically bonded residue pairs ($j = i \pm 1$) are excluded. The addition of E_{col} penalizes steric collisions between residues whose C_α atoms are within a distance of R_{col}.

With the addition of the collision energy, the SPs are solved by setting $\nabla F(E_{ENM1} + E_{col}, E_{ENM2} + E_{col}) = 0$ which is equivalent to solving the following SP equation (the SP is represented by X_{SP}):

$$\lambda\nabla E_{ENM1}(X_{SP}) + (1-\lambda)\nabla E_{ENM2}(X_{SP}) + \nabla E_{col}(X_{SP}) = 0, \quad (8)$$

As λ varies from 1 to 0, X_{SP} traces a pathway that connects the beginning and end conformations of a transition. Because this pathway passes all possible SPs, it gives a "universal" minimum-energy path regardless of the detailed form of $F(E_1, E_2)$.[46] iENM will output the above pathway as the predicted pathway for the given transition.

We solve Eq. (8) by using the following iterative procedure to find the minima of the linearly interpolated potential function $\lambda E_{ENM1} + (1-\lambda) E_{ENM2} + E_{col}$ with the Newton-Raphson method:

1. Initialization: set $n=0$, $X_{SP,0} = X_1$, which is the C_α coordinates of the beginning conformation.
2. Given $X_{SP,n}$, calculate $\lambda = \lambda_n = -\frac{[\nabla E_{ENM1}-\nabla E_{ENM2}]\cdot[\nabla E_{ENM2}+\nabla E_{col}]}{|\nabla E_{ENM1}-\nabla E_{ENM2}|^2}$ to minimize $|\lambda\nabla E_{ENM1} + (1-\lambda)\nabla E_{ENM2} + \nabla E_{col}|$.
3. Calculate $R_n = \lambda_n \nabla E_{ENM1} + (1-\lambda_n)\nabla E_{ENM2} + \nabla E_{col}$.
4. If $|R_n| < 0.00001$, go to Step 7.
5. Displace $X_{SP,n}$ by

$$\delta X_{SP} = -[\lambda_n H_1 + (1-\lambda_n)H_2 + H_{col}]^{-1}R_n, \quad (9)$$

where H_1, H_2, and H_{col} are the Hessian matrices calculated for E_{ENM1}, E_{ENM2}, and E_{col} [see Eq. (3)].
6. Go to Step 3.
7. Calculate

$$X_{SP,n+1} = X_{SP,n} + \delta X_{SP} \text{ and } \delta X_{SP} \sim -\delta\lambda[\lambda_n H_1 + (1-\lambda_n)H_2 + H_{col}]^{-1}[\nabla E_{ENM1} - \nabla E_{ENM2}], \quad (10)$$

where H_1, H_2, and H_{col} are the Hessian matrices calculated for E_{ENM1}, E_{ENM2}, and E_{col} [see Eq. (3)], and $\delta\lambda$ is chosen so that the magnitude of δX_{SP} is small (i.e.$|\delta X_{SP}|/\sqrt{N} < 0.1$Å).
8. Stop if $X_{SP,n+1}$ has reached X_2 which is the C_α coordinates of the end conformation, otherwise set $n \leftarrow n+1$, then go to Step 2.

The solutions of linear equations in Eqs. (9) and (10) are obtained using a sparse linear equation solver CHOLMOD.[53] In Eq. (10) we compute an incremental structural displacement δX_{SP} based on the force-induced linear responses—δX_{SP} is calculated as a weighted sum of all normal modes of the Hessian matrix $\lambda_n H_1 + (1-\lambda_n)H_2 + H_{col}$. Because the weight of each normal mode is inversely proportional to its eigenvalue, the collective

motions described by the lowest modes are favorably sampled along the transition pathway.

Transition Pathway Modeled by Mixed-ENM

In a previous study,[46] we solved Eq. (6) approximately by using the following 2nd order expansion of an ENM potential:

$$E_{\mathrm{ENM1}}(X) \approx \frac{1}{2}(X^T - X_1^T)H_1(X - X_1)$$
$$E_{\mathrm{ENM2}}(X) \approx \frac{1}{2}(X^T - X_2^T)H_2(X - X_2), \quad (11)$$

where H_1 (H_2) is the Hessian matrix calculated for E_{ENM1} (E_{ENM2}) at the beginning conformation X_1 (end conformation X_2).

The approximate solution of Eq. (6)[46] is

$$X_{\mathrm{SP}} = [\lambda H_1 + (1-\lambda)H_2]^{-1}[\lambda H_1 X_1 + (1-\lambda)H_2 X_2]. \quad (12)$$

To remove the contributions of translational and rotational modes for the beginning and end conformations, we project out the eigenvectors of these modes from X_{SP}. As λ varies from 1 to 0, X_{SP} traces a pathway that connects the beginning and end conformations of a transition.[46]

Assessment of Transition Progress Using Reaction Coordinates

The predicted transition pathway allows us to determine the order of conformational changes involving different parts of a protein (for example, the ATP-binding site which pertains to the biochemical processes of ATP binding, hydrolysis and product release). For this purpose, the following reaction coordinate (RC) is defined for an intermediate conformation of a given part S[54]:

$$RC_S = (\delta X_S \bullet \delta X_{S,\mathrm{obs}}) \Big/ \left|\delta X_{S,\mathrm{obs}}\right|^2, \quad (13)$$

where δX_S is the displacement vector of part S from the beginning conformation of a transition to a given intermediate conformation, and $\delta X_{S,\mathrm{obs}}$ is the observed displacement of part S from the beginning conformation to the end conformation of a transition. RC_S measures the motional progress of part S in the direction of a transition. $RC_S = 0$ at the beginning of a transition, and $RC_S = 1$ at the end of a transition. For two different parts (named S_1 and S_2) in an intermediate conformation, if $RC_{S_1} > RC_{S_2}$, then S_1's movement precedes S_2's movement.

We choose to use the reaction coordinate rather than RMSD when comparing predicted pathways with experimental structures for the following reason. The reaction coordinate focuses on the structural motions along the direction of a conformational transition [given by $\delta X_{S,\mathrm{obs}}$ in Eq. (13)], while the motions/fluctuations orthogonal to $\delta X_{S,\mathrm{obs}}$ are excluded. Therefore, it allows us to deduce the motional order along the direction of a transition despite large fluctuations in orthogonal directions which are probably present in a large set of experimental structures solved under different conditions (various crystal symmetries, mutations, ligands, etc). So a small RMSD from experimental structures may not be expected for a correctly predicted pathway. Indeed, we have found only slight reduction of minimal RMSD from experimental structures when comparing the iENM pathways with alternative ones generated by mixed-ENM and morph server (see Supporting Information Fig. S1).

RESULTS

We will first show the improvement of iENM over mixed-ENM in generating an energetically favorable pathway. Then, we will apply iENM to the ATP-driven conformational transitions in three biological nanomachines (myosin,[12] F_1 ATPase,[13] and GroEL[14]). We will critically assess the iENM-predicted transition pathways by predicting the order of local and global conformational changes in these tiny motors. The predictions will be evaluated in comparison with the order of structural events deduced from the experimental structures of these proteins.

Energetic comparison between iENM pathway and mixed-ENM pathway

To assess the energetic favorability of iENM pathways, we have calculated two ENM potential functions based on the beginning and end conformations of a transition (E_{ENM1} and E_{ENM2}), and the linearly interpolated energy $\lambda E_{\mathrm{ENM1}} + (1-\lambda)E_{\mathrm{ENM2}}$. The energy calculations are done for the intermediate conformations along the transition pathways generated by iENM and mixed-ENM. In all three cases (myosin,[12] F_1 ATPase,[13] and GroEL[14]), the intermediate conformations of the iENM pathway have lower energy than that of the mixed-ENM pathway (see Fig. 1). This improvement is attributed to the more accurate calculation of ENM potential energy by iENM than mixed-ENM (the latter is based on the approximation given in Eq. (11) of Methods). Although the ENM potential energy does not accurately describe the chemical interactions in a protein structure, it gives a reasonable assessment of deviations from the native-like C_α–C_α distances between residues in contact. Therefore, the iENM pathway is energetically more favorable than the mixed-ENM pathway by better preserving the native-like residue-residue contacts in both the beginning and end conformations of a transition. Nevertheless, energetic

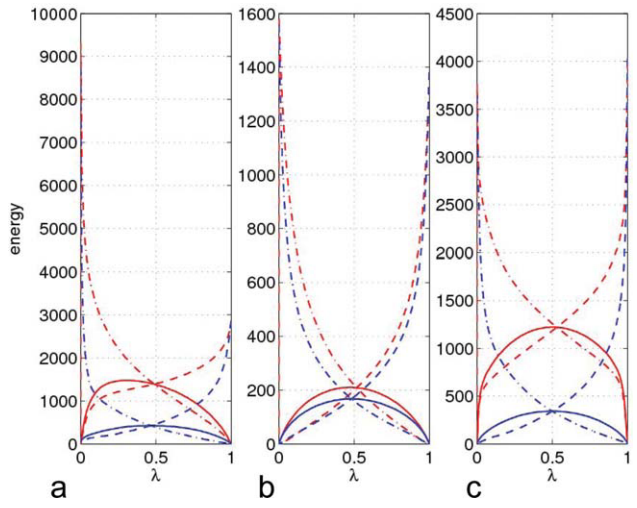

Figure 1

Energy of intermediate conformations along the iENM (blue) and mixed-ENM (red) transition pathways for (**a**) myosin's recovery stroke; (**b**) open-to-close transition of F_1 ATPase; (**c**) *T*-to-*R*″ transition of chaperonin GroEL. The ENM potential energy based on the beginning conformation [E_{ENM1}, see Eq. (1)], the end conformation [E_{ENM2}, see Eq. (1)], and the linearly interpolated energy $\lambda E_{ENM1} + (1 - \lambda)E_{ENM2}$ are shown as dash-dot, dashed and solid lines. [Color figure can be viewed in the online issue, which is available at www.interscience.wiley.com.]

favorability alone does not validate the correctness of a predicted pathway. Next, we will perform a more stringent test of the iENM pathways by using experimental structures of myosin,[12] F_1 ATPase,[13] and GroEL.[14]

Myosin's transition of recovery stroke

Myosins[12], a superfamily of actin-based ATP-powered motor proteins, are involved in diverse functions ranging from muscle contraction to intracellular transportation.[55] Myosin has been under extensive investigations by biochemical, biophysical, genetic and structural studies (see reviews[56–58]). Mounting evidence has outlined a mechano-chemical coupling mechanism involving a cascade of ATP-driven conformational transitions between a series of biochemical states—these conformational transitions are thought to orchestrate allosteric couplings among actin binding/release, ATPase events and force generation. The primary kinetic cycle of a monomeric actomyosin has been outlined by extensive kinetic studies,[59–61] which consists of at least six biochemical states:

$$\text{A-M} \rightarrow \text{A-M-ATP} \rightarrow \text{M-ATP} \rightarrow \text{M-ADP-Pi} \rightarrow \text{A-M-ADP-Pi} \rightarrow \text{A-M-ADP} \rightarrow \text{A-M}$$

(A : actin, M : myosin, Pi : γ-phosphate)

Starting from the nucleotide-free A-M state (rigor state), ATP binding dissociates myosin from actin. Then ATP hydrolysis leads to a transition from the M-ATP state to the M-ADP-Pi state, which is accompanied by an upward rotation of a lever arm (the force-generating component of myosin) to a primed position (named recovery stroke). Next, actin binding accelerates Pi release from myosin, resulting in force generation (powerstroke) as the lever arm rotates downward.[56–58] Subsequent release of ADP returns myosin to the A-M state for the next cycle.

For the lack of actin-bound myosin crystal structures, we will focus on the transition from M-ATP state to M-ADP-Pi state, which occurs when myosin is detached from actin. During this transition, ATP hydrolysis is accompanied by the closing of its active site [comprised of highly conserved ATP-binding motifs including P loop, switch I and switch II, see Fig. 2(a)], and an upward rotation of the converter subdomain [see Fig. 2(a)] which primes the lever arm for subsequent force generation.[56–58] It is widely believed that the above conformational changes are allosterically coupled via a number of key structural elements—including several flexible joints [62] [such as relay helix and SH1 helix, see Fig. 2(a)], and a central β-sheet.[63–66]

The conformational couplings and transitions in myosin have been investigated by ENM in previous studies.[46,54,67–70] Although the recovery stroke has been studied by various computational methods,[71–77] the causal relationship between various structural events remains controversial. Fischer *et al.* simulated a minimal-energy pathway from M-ATP state to M-ADP-Pi state, which showed that the closing of switch II at the active site triggers an amplifying cascade of conformational changes along the relay helix toward the converter.[71] Alternatively, Cui and coworkers performed a targeted MD simulation from M-ATP state to M-ADP-Pi state, which suggested that the local conformational change at active site that allows ATP hydrolysis is gated by and therefore follows the rotation of converter.[72]

To resolve the above controversy, we have generated an iENM transition pathway from a *Dictyostelium* myosin structure at M-ATP state (PDB code: 1FMW) to one at M-ADP-Pi state (PDB code: 1VOM). The missing residues of the two crystal structures are added by the MODLOOP server.[78] Then we have calculated the reaction coordinates (RC_{local} and RC_{global}, see Methods) for the active site (residues 179-186, 233-238, and 454-459) and the myosin motor domain (residues 81-747, after excluding the weakly conserved SH3 domain of the N-terminal subdomain) to quantify the progress of their conformational changes during the transition. The above calculations are performed not only for the intermediate conformations along the iENM pathway, but also for 85 intermediate crystal structures of various myosins gleaned from Protein Data Bank (see Supporting Information Table S1). The myosin crystal structures are assigned to three biochemical states (M-ATP, M-ADP-Pi, A-M state) based on the

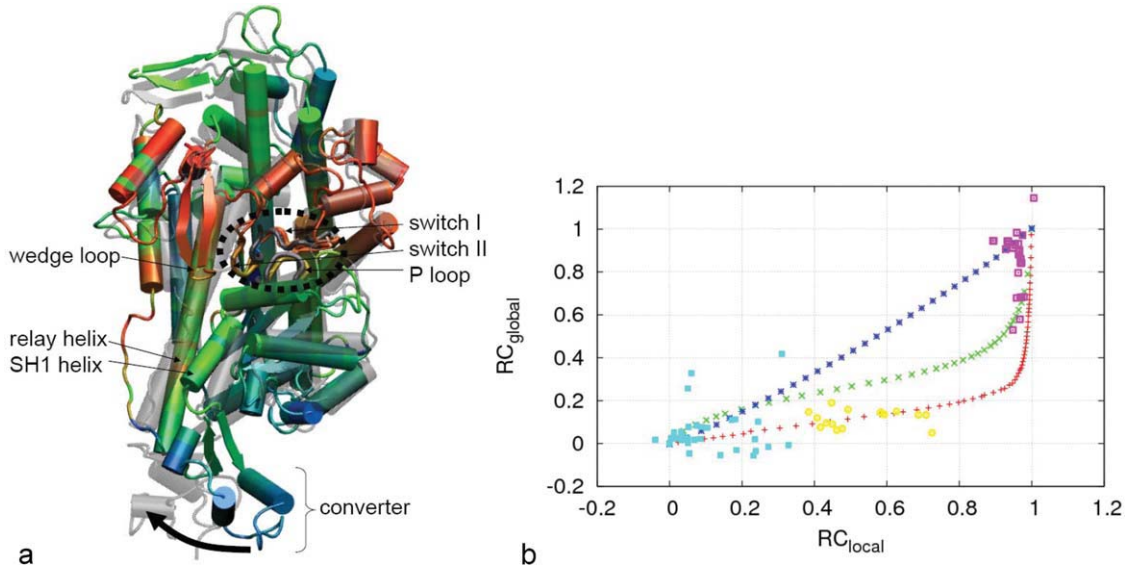

Figure 2

Results of transition pathway modeling for myosin's recovery stroke: (**a**) Superposition of the beginning conformation (PDB code: 1FMW, shown as opaque cartoons) and the end conformation (PDB code: 1VOM, shown as transparent cartoons) of the transition: residues in the beginning conformation are colored according to their motional order (for example, early-moving residues are colored red, late-moving ones are colored blue, intermediate ones are colored green), the active-site residues are circled and shown as thick tubes, key structural components are labeled, an upward rotation of converter is shown by a curved arrow. (**b**) Local and global reaction coordinates (RC_{local} and RC_{global}) for intermediate conformations on iENM pathway (red), mixed-ENM pathway (green) and morph-server-generated pathway (blue), and myosin crystal structures at M-ATP state (cyan), M-ADP-Pi state (purple), A-M state (yellow). RC_{local} (RC_{global}) quantifies the progress of conformational change of active site (entire myosin motor domain) along a transition pathway—it is 0 for the beginning conformation and 1 for the end conformation.

RMSD of active-site residues relative to three representative myosin structures (PDB code: 1FMW, 1VOM, 1W8J).

The iENM pathway overlaps well with the myosin crystal structures at M-ATP state and M-ADP-Pi state on the RC-plane [see Fig. 2(b)], and they are distributed within the region where $RC_{local} > RC_{global}$ (except for three outliers, including two switch II-mutants (PDB code: 1W9I and 1W9K)). So we infer that the local conformational change (closing of active site) precedes the global conformational change of myosin motor domain (dominated by a large rotation of converter). In comparison, the mixed-ENM pathway suggests a qualitatively similar order of local and global structural events, although it does not overlap well with the crystal structures at M-ATP state [see Fig. 2(b)]. As a control, we have also assessed an interpolated pathway generated by a popular morph server,[79] which predicts synchronized progressing of both local and global conformational changes and deviates significantly from the crystal structures on the RC-plane [see Fig. 2(b)].

To map the motional order of individual residues along the iENM pathway, we use the following procedure: first, we determine for each residue its 'crossover conformation' on the iENM pathway where the residue's C_α atom is at equal distance from its beginning and end positions of the transition; then, we sort all residues according to the order of their crossover conformations along the iENM pathway. In agreement with the results of RC calculations [see Fig. 2(b)], the motions of ATP-binding residues (such as switch I and switch II) occur early, while the motions of converter residues occur late [see Fig. 2(a)]. Interestingly, the motions of the wedge loop and the N-terminus of relay helix also occur early during the transition [see Fig. 2(a)], which agrees with a recent study that found the local transitions in these structural elements are required for turning on the ATPase activity.[73]

Our finding is consistent with a causal relationship by which ATP hydrolysis causes a subsequent upward rotation of the converter,[71] which is energetically more favorable than an alternative order by which an upward rotation of the converter precedes the closing of active site.[72] Our finding agrees with a previous simulation of recovery stroke using a minimal-energy pathway,[71] but not with another simulation study based on Targeted MD.[72] One caveat of the minimal-energy pathway is its lack of consideration of structural fluctuations.[72] Although structural fluctuations are not explicitly considered in iENM, given the coarse-grained nature and robustness of ENM,[43] we think it is unlikely that structural fluctuations would qualitatively alter the iENM-predicted pathway. The finding of good agreement with myosin crystal structures [see Fig. 2(b)] further supports the qualitative correctness of iENM pathway.

It is interesting that the myosin crystal structures assigned to the A-M state (rigor-like state[63–66]) also fall on the iENM pathway [see Fig. 2(b)]. Because the A-M state can be viewed as an intermediate state during the reverse transition from M-ADP-Pi state to M-ATP state, we infer that a reversed sequence of structural events may occur during the above transition. Namely, the downward rotation of converter precedes the opening of active site that allows the release of Pi and ADP.[80,81] A more realistic modeling of the above transition requires a proper treatment of actin-myosin binding,[54] which is beyond the scope of this study.

Open-to-close transition of F_1 ATPase

F_1 ATPase[13] (referred to as F_1 hereafter) is a globular catalytic moiety of F_0F_1-ATP synthase, a giant supramolecular machine that utilizes the energy of proton motive force across the mitochondrial membrane to synthesize ATP (see a recent review[82]). F_1 forms a hexamer ($\alpha_3\beta_3$) consisting of three β subunits sandwiched between three α subunits,[13] which encloses a central stalk comprised of γδϵ subunits.[83] Three catalytic sites and three non-catalytic sites are located at the interfaces between adjacent α and β subunits.[13] The former are comprised of highly conserved catalytic residues from β subunit (including Walker A or P loop motif[84]) and α subunit. F_1 hydrolyzes ATP to generate a counterclockwise rotation of γ subunit (as viewed from membrane).[85]

Decades of biochemical studies have found that nucleotide binding and hydrolysis are highly cooperative among the three catalytic sites in F_1.[86–89] To account for the cooperative ATPase in F_1, a "binding change" mechanism[90] has been proposed and widely accepted. It postulates that the γ subunit rotates during ATP hydrolysis to facilitate a cooperative change in the nucleotide-binding affinity of three catalytic sites. High resolution structural studies have offered critical support to the binding change mechanism. The landmark crystal structure of bovine F_1[13] (PDB code: 1BMF) has captured a snapshot of three structurally distinct catalytic sites. The empty E-site, AMPPNP-bound TP-site and ADP-bound DP-site are located at α_E-β_E, α_{TP}-β_{TP} and α_{DP}-β_{DP} interface, respectively.[13] E-site and β_E subunit adopt an open conformation.[13] TP-site, DP-site, and associated β subunits (β_{TP} and β_{DP}) are in a closed conformation.[13] A cyclic conformational transition is thought to convert E-site, TP-site and DP-site to TP-site, DP-site and E-site and lead to a 120° rotation of γ subunit.[13] However, the dynamic details of this transition remain unclear. In complement with the crystal structures of F_1, single-molecule imaging studies have offered valuable information for F_1 dynamics. The γ subunit undergoes a 120° rotation per ATP hydrolyzed,[91,92] which is resolved into four stages: ATP-waiting dwell, 80° substep following ATP binding, catalytic dwell, and 40° substep linked to the release of a hydrolysis product.[93,94] During the 120° γ rotation, ATP binding and cleavage occur at two different catalytic sites,[94] and a third catalytic event occurs at a third site.[95] Thus all three catalytic sites participate sequentially to drive the 120° γ rotation.[95]

A variety of computational methods have been applied to F_1 including kinetic modeling[96,97] and structure-based molecular simulations. All-atom molecule simulations were utilized in free energy calculations of nucleotide binding,[98,99] QM/MM calculations of catalysis,[100,101] and MD simulations of structural changes in F_1.[102–105] Recently, coarse-grained models, including Go model[106] and ENM,[107,108] have been employed to simulate conformational transitions in F_1. A popular mechanistic model of F_1 postulates that ATP binding, by progressively forming hydrogen bonds between ATP and P loop,[109] drives an open-to-close conformational change of β_E subunit which subsequently pushes γ subunit to rotate like a camshaft.[110] However, it remains unknown at atomic or residue level how the binding and release of nucleotide are coupled to the global conformational changes in F_1.[106–108]

To probe the allosteric coupling between nucleotide binding and the global conformational change in a β subunit of F_1, we have generated an iENM transition pathway from the open conformation (β_E) to the closed conformation (β_{TP}) of β subunit in a bovine F_1 structure (PDB code: 1BMF). Then we have calculated the reaction coordinates (RC_{local} and RC_{global}, see Methods) for the active site (residues 159–164, 186–188, 256–259, and 308-309[111]) and the entire β subunit to quantify the progress of their conformational changes during the transition. The above calculations are performed not only for the intermediate conformations along the iENM pathway, but also for 92 crystal structures of F_1's β subunit gleaned from Protein Data Bank (see Supporting Information Table S2). The β subunit crystal structures are assigned to two biochemical states (nucleotide-free state and nucleotide-bound state) based on the RMSD of active-site residues relative to two representative β subunit structures (PDB code: 1BMF, β_E and β_{TP} subunits).

The iENM pathway is distributed within the region where $RC_{local} > RC_{global}$ [see Fig. 3(b)], which indicates that the closing of catalytic site (E-site) precedes the open-to-close conformational change in β subunit. While most β subunit crystal structures are distributed near (0,0) or (1,1) on the RC-plane [see Fig. 3(b)], one ADP:AlF_4^--bound structure (PDB code: 1H8E, chain E) with a half-closed catalytic site[112] is located far from (0,0) and (1,1), and it sits right on the iENM pathway [see Fig. 3(b)], which lends support to the order of structural events predicted by iENM. In comparison, the mixed-ENM pathway predicts a qualitatively similar order of local and global structural events, although it deviates slightly from the ADP: AlF_4^--bound β subunit structure[112] [see Fig. 3(b)]. As a control, we have also

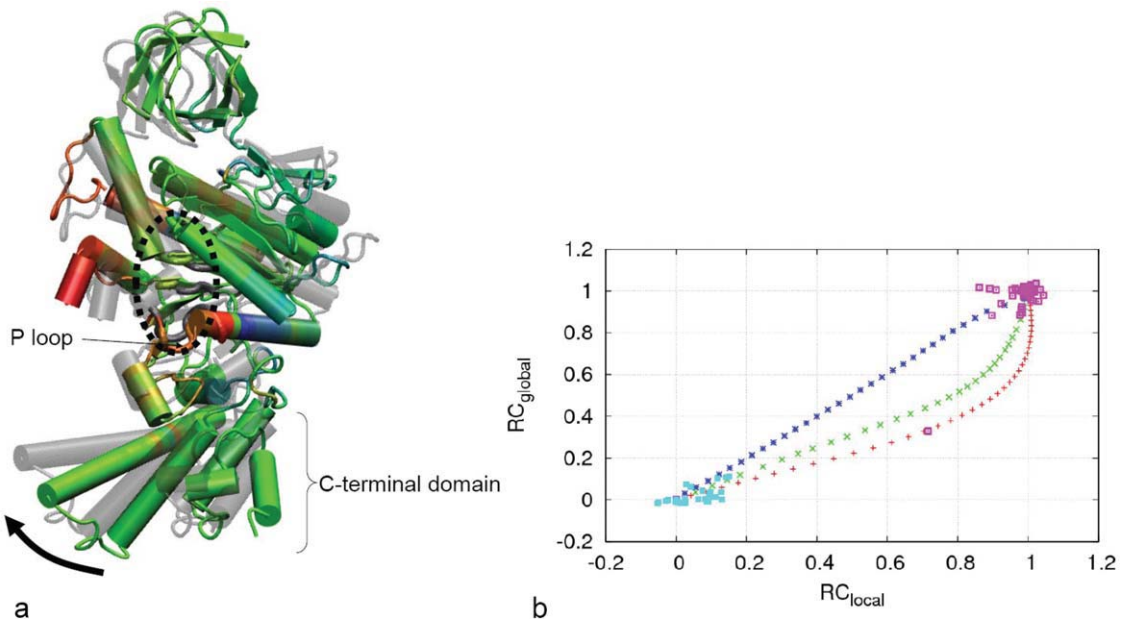

Figure 3

Results of transition pathway modeling for the open-to-close transition of F_1 ATPase: (**a**). Superposition of the beginning conformation (PDB code: β_E subunit of 1BMF, shown as opaque cartoons) and the end conformation (PDB code: β_{TP} subunit of 1BMF, shown as transparent cartoons) of the transition: residues in the beginning conformation are colored according to their motional order (for example, early-moving residues are colored red, late-moving ones are colored blue, intermediate ones are colored green), the active-site residues are circled and shown as thick tubes, key structural components are labeled, a large rotation of the C-terminal domain is shown by a curved arrow. (**b**). Local and global reaction coordinates (RC_{local} and RC_{global}) for intermediate conformations on iENM pathway (red), mixed-ENM pathway (green), morph-server-generated pathway (blue), and crystal structures of F_1's β subunit at nucleotide-free state (cyan), nucleotide-bound state (purple). RC_{local} (RC_{global}) quantifies the progress of conformational change of active site (entire β subunit) along a transition pathway—it is 0 for the beginning conformation and 1 for the end conformation.

assessed an interpolated pathway generated by the morph server,[79] which predicts synchronized progressing of both local and global conformational changes [see Fig 3(b)]. To map the motional order of individual residues along the iENM pathway, we sort all residues according to their crossover conformations [see Fig. 3(a)]. In agreement with the results of RC calculations [see Fig. 3(b)], the local motions of P loop residues occur early, while the open-to-close motions of residues on the C-terminal subdomain occur later during the transition.

To probe the allosteric coupling between nucleotide release and the global conformational change in a β subunit of F_1, we have generated an iENM pathway from the closed conformation (β_{DP}) to the open conformation (β_E) of β subunit in a bovine F_1 structure (PDB code: 1BMF). Because of the high similarity between β_{DP} and β_{TP} conformations, this transition pathway is essentially the reverse of the iENM pathway of the open-to-close transition ($\beta_E \rightarrow \beta_{TP}$). Therefore, we infer that the opening of catalytic site (DP-site) follows the close-to-open conformational change in β subunit.

Taken together, the above findings imply the following two causal relationships between nucleotide binding/release and the global conformational changes in a β subunit: 1. the closing of E-site induced by ATP binding leads to the open-to-close conformational change of β_E subunit; 2. the close-to-open conformational change of β_{DP} subunit leads to the opening of DP-site that allows ADP release. If we further assume that the global conformational changes in β_{DP}/β_E subunit are mechanically coupled to the rotation of γ subunit (akin to a camshaft[110]), then our finding supports the presence of an intermediate F_1 state with all three catalytic sites occupied by nucleotides, which is in agreement with the tri-site model of F_1.[107,108,113]

T-to-*R*′ transition of Chaperonin GroEL

E. coli. chaperonin GroEL is the most extensively studied molecular chaperone that assists protein folding.[14] It consists of two heptameric rings stacked back-to-back.[114] During its reaction cycle, GroEL goes through a number of biochemical states as triggered by ATPase activity and interactions with the cochaperonin GroES.[14,115] Beginning from the nucleotide-free T state, a substrate protein is recognized and bound by GroEL. Then ATP binding leads to a transition from the *T* state to the *R* state. Next the binding of GroES and ATP hy-

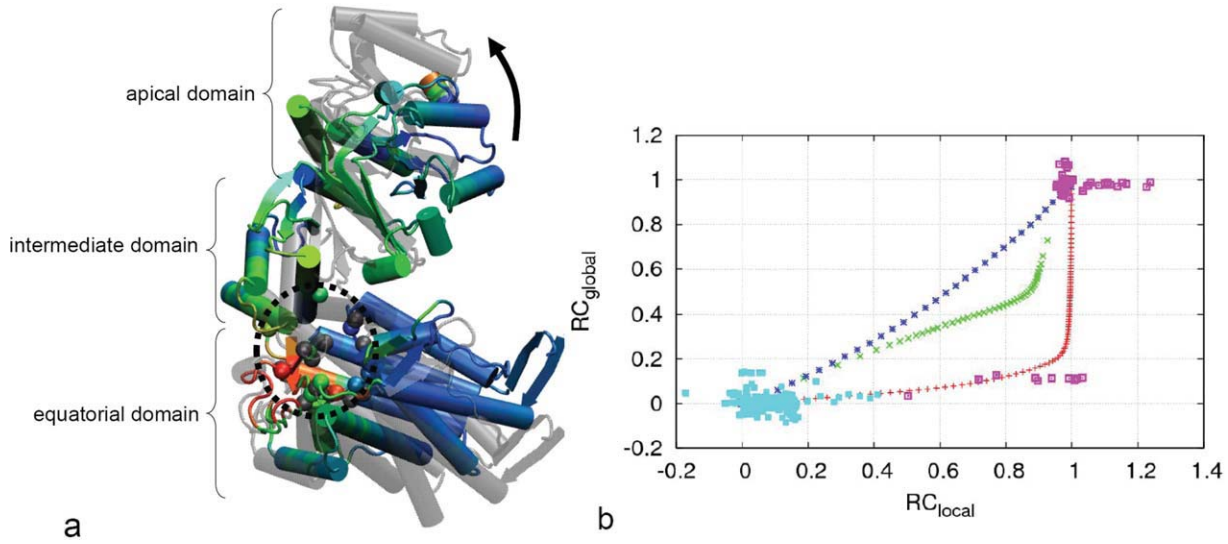

Figure 4

Results of transition pathway modeling for the *T*-to-*R*″ transition of chaperonin GroEL: (**a**) Superposition of the beginning conformation (PDB code: chain H of 1AON, shown as opaque cartoons) and the end conformation (PDB code: chain A of 1AON, shown as transparent cartoons) of the transition: residues in the beginning conformation are colored according to their motional order (for example, early-moving residues are colored red, late-moving ones are colored blue, intermediate ones are colored green), the active-site residues are circled and shown as spheres, key structural components are labeled, a large displacement of the apical domain is shown by a curved arrow. (**b**) Local and global reaction coordinates (RC_{local} and RC_{global}) for intermediate conformations on iENM pathway (red), mixed-ENM pathway (green), morph-server-generated pathway (blue), and experimental structures of GroEL at *T* state (cyan), *R*/*R*″ state (purple). RC_{local} (RC_{global}) quantifies the progress of conformational change of active site (entire GroEL subunit) along a transition pathway—it is 0 for the beginning conformation and 1 for the end conformation.

drolysis lead to the *R*″ state.[14,115] The $T \rightarrow R \rightarrow R''$ allosteric transitions result in the formation of the *cis*-ring which encapsulates the substrate protein. When ATP binds to the opposite ring (*trans* ring) the ligands (the inorganic phosphate, ADP and GroES) are ejected from the *cis* ring. The crystal structure of GroEL-GroES complex[114] at *R*″*T* state and cryo-EM structures of GroEL at *R* state[116] have offered a glimpse to the structural states of GroEL. The large conformational changes from T state to *R*″ state involve a large twisting and upward displacement of the apical domain and a downward movement of the intermediate domain associated with the closing of active site[114] [see Fig. 4(a)]. Many computational studies have been performed to investigate the conformational dynamics of GroEL.[117–133]

To probe the allosteric coupling between ATP binding/hydrolysis and the global conformational change in a subunit of GroEL, we have generated an iENM transition pathway from the T state conformation (PDB code: 1AON, chain H) to the *R*″ state conformation (PDB code: 1AON, chain A) of a GroEL subunit. Then we have calculated the reaction coordinates (RC_{local} and RC_{global}, see Methods) for the active site (residues 31–33, 87, 91, 150, 151, 398, 415, 454, 479–481, 493, 495[114]) and the entire subunit to quantify the progress of their conformational changes during the transition. The above calculations are performed for the intermediate conformations along the iENM pathway, and also for 370 experimental structures of GroEL gleaned from Protein Data Bank (see Supporting Information Table S3). The experimental structures are assigned to T state and *R*/*R*″ state based on the RMSD of active-site residues relative to two representative structures (PDB code: 1AON, chains H and A).

The iENM pathway overlaps well with the experimental structures at T state and *R*/*R*″ state on the RC-plane, including several ATP-bound R-state structures of GroEL[116] which are far from (0,0) or (1,1) [see Fig. 4(b)]. Because the iENM pathway and experimental structures are mostly distributed within the region where $RC_{local} > RC_{global}$ (except for a few outliers near (0,0) and (1,1)), we infer that the local conformational change (closing of active site) precedes the global conformational change of GroEL (dominated by a large twisting and upward displacement of apical domain). In comparison, the mixed-ENM pathway predicts a qualitatively similar order of local and global structural events, although it does not overlap well with the R-state experimental structures[116] [see Fig. 4(b)]. As a control, we have also assessed an interpolated pathway generated by the morph server,[79] which predicts synchronized progressing of both local and global conformational changes and deviates significantly from the experimental structures [see Fig. 4(b)]. To map the motional order of individual residues along the iENM pathway, we sort all residues

according to their crossover conformations [see Fig. 4(a)]. In agreement with the results of RC calculations [see Fig. 4(b)], the motions of several ATP-binding residues [including residues 32, 150, 493, see Fig. 4(a)] occur early, the motions of residues in apical domain and equatorial domain occur late, while the motions of residues in intermediate domain occur in between the above two.

Therefore, our finding supports a causal relationship by which ATP binding induces the global conformational change that allows encapsulation of a substrate protein. Our finding agrees with the result of a targeted MD simulation which predicted a two-step transition in GroEL.[118] Namely, the early downward motion of the intermediate domain induced by ATP binding triggers the larger movements of the apical and equatorial domains.[118]

The same iENM pathway works for the reverse transition ($R'' \rightarrow T$), which predicts that the large movement of apical domain precedes the opening of active site. Taken together, we can infer the following allosteric coupling between nucleotide binding of *trans* ring and nucleotide release of *cis* ring in GroEL: ATP binding to the *trans* ring causes large conformational changes in the apical and equatorial domains of the *trans* ring, which subsequently propagate to the *cis* ring (via tilting of the equatorial domain[117,120]), and eventually induce the opening of active sites in the *cis* ring that releases ADP. A possible test of the above prediction is to trap GroEL-GroES complex in a crystalline state with both rings bound to 14 nucleotides.

DISCUSSION AND CONCLUSION

Instead of directly simulating the atomic motions during a protein conformational transition, we aim to qualitatively outline the order of structural events involving various parts of a protein complex undergoing the transition. The understanding of order of local vs. global structural events will shed light on two competing models for motor protein functions:

1. Power-stroke model[56–58] postulates that the global mechanical motions are driven by chemical events such as ATP binding, hydrolysis or product release. It implies that the local conformational change at active site precedes the global conformational change responsible for mechanical movement;
2. Brownian ratchet model postulates that the global mechanical motions are driven by thermal fluctuations and gated by chemical events, which implies that the local conformational change at active site follows the global conformational change and locks the new global conformation[72] (assuming the local conformational change at active site is accompanied by a chemical event like ligand binding, which may not be true if, for example, the ligand-bound active-site conformation is sampled in the absence of ligand).

Therefore, our finding seems to agree with the order of local and global conformational changes predicted by the power-stroke model instead of the Brownian ratchet model. However, we cannot rule out the latter model because iENM cannot resolve whether a conformational transition is driven by chemical energy or thermal energy (Note: iENM does not model ligand binding explicitly and neither does it take thermal fluctuations into account). It is conceivable that both chemical and thermal energy may be utilized to assist the barrier-crossing events of a conformational transition. So both models may be relevant to motor protein functions.

In conclusion, by sampling a double-well potential function constructed from two elastic network models based on the beginning and end conformations of a transition, we have developed an interpolated elastic network model to generate a transition pathway between the two protein conformations, which is independent of the specific form of the double-well potential function. For validation, we have predicted the order of local and global conformational changes during key ATP-driven transitions in three important biological nanomachines (myosin, F_1 ATPase and chaperonin GroEL). We have found that the local conformational change associated with the closing of active site precedes the global conformational change leading to mechanical motions. Our finding is in good agreement with the distribution of intermediate experimental structures, and it supports the importance of local motions at active site to drive (via a power-stroke mechanism) or gate (via a Brownian ratchet mechanism) various conformational transitions underlying the workings of a diverse range of biological nanomachines. The iENM method will be made available at a webserver (enm.lobos.nih.gov).

REFERENCES

1. Henzler-Wildman K, Kern D. Dynamic personalities of proteins. Nature 2007;450:964–972.
2. Gerstein M, Echols N. Exploring the range of protein flexibility, from a structural proteomics perspective. Curr Opin Chem Biol 2004;8:14–19.
3. Yon JM, Perahia D, Ghelis C. Conformational dynamics and enzyme activity. Biochimie 1998;80:33–42.
4. Yang LW, Bahar I. Coupling between catalytic site and collective dynamics: a requirement for mechanochemical activity of enzymes. Structure 2005;13:893–904.
5. Tobi D, Bahar I. Structural changes involved in protein binding correlate with intrinsic motions of proteins in the unbound state. Proc Natl Acad Sci USA 2005;102:18908–18913.
6. Kern D, Zuiderweg ER. The role of dynamics in allosteric regulation. Curr Opin Struct Biol 2003;13:748–757.
7. Gunasekaran K, Ma B, Nussinov R. Is allostery an intrinsic property of all dynamic proteins? Proteins 2004;57:433–443.

8. Changeux JP, Edelstein SJ. Allosteric mechanisms of signal transduction. Science 2005;308:1424–1428.
9. Swain JF, Gierasch LM. The changing landscape of protein allostery. Curr Opin Struct Biol 2006;16:102–108.
10. Cui Q, Karplus M. Allostery and cooperativity revisited. Protein Sci 2008;17:1295–1307.
11. Goodey NM, Benkovic SJ. Allosteric regulation and catalysis emerge via a common route. Nat Chem Biol 2008;4:474–482.
12. Berg JS, Powell BC, Cheney RE. A millennial myosin census. Mol Biol Cell 2001;12:780–794.
13. Abrahams JP, Leslie AGW, Lutter R, Walker JE. Structure at 2.8-angstrom resolution of F1-Atpase from bovine heart-mitochondria. Nature 1994;370:621–628.
14. Sigler PB, Xu ZH, Rye HS, Burston SG, Fenton WA, Horwich AL. Structure and function in GroEL-mediated protein folding. Annu Rev Biochem 1998;67:581–608.
15. Kay LE. NMR studies of protein structure and dynamics. J Magn Reson 2005;173:193–207.
16. Boehr DD, Dyson HJ, Wright PE. An NMR perspective on enzyme dynamics. Chem Rev 2006;106:3055–3079.
17. Schotte F, Lim MH, Jackson TA, Smirnov AV, Soman J, Olson JS, Phillips GN, Wulff M, Anfinrud PA. Watching a protein as it functions with 150-ps time-resolved X-ray crystallography. Science 2003;300:1944–1947.
18. Hayward S, Lee RA. Improvements in the analysis of domain motions in proteins from conformational change: DynDom version 1.50. J Mol Graph Model 2002;21:181–183.
19. Wriggers W, Schulten K. Protein domain movements: detection of rigid domains and visualization of hinges in comparisons of atomic coordinates. Proteins 1997;29:1–14.
20. Jacobs DJ, Rader AJ, Kuhn LA, Thorpe MF. Protein flexibility predictions using graph theory. Proteins 2001;44:150–165.
21. Daily MD, Gray JJ. Local motions in a benchmark of allosteric proteins. Proteins 2007;67:385–399.
22. Najmanovich R, Kuttner J, Sobolev V, Edelman M. Side-chain flexibility in proteins upon ligand binding. Proteins 2000;39:261–268.
23. Betts MJ, Sternberg MJE. An analysis of conformational changes on protein-protein association: implications for predictive docking. Protein Eng 1999;12:271–283.
24. Henzler-Wildman KA, Lei M, Thai V, Kerns SJ, Karplus M, Kern D. A hierarchy of timescales in protein dynamics is linked to enzyme catalysis. Nature 2007;450:U913–U927.
25. Gerstein M, Krebs W. A database of macromolecular motions. Nucleic Acids Res 1998;26:4280–4290.
26. Kim MK, Jernigan RL, Chirikjian GS. Efficient generation of feasible pathways for protein conformational transitions. Biophys J 2002;83:1620–1630.
27. Karplus M, McCammon JA. Molecular dynamics simulations of biomolecules. Nat Struct Biol 2002;9:646–652.
28. Schlitter J, Engels M, Kruger P. Targeted molecular-dynamics—a new approach for searching pathways of conformational transitions. J Mol Graph 1994;12:84–89.
29. Paci E, Karplus M. Forced unfolding of fibronectin type 3 modules: an analysis by biased molecular dynamics simulations. J Mol Biol 1999;288:441–459.
30. Klepeis JL, Lindorff-Larsen K, Dror RO, Shaw DE. Long-timescale molecular dynamics simulations of protein structure and function. Curr Opin Struct Biol 2009;19:120–127.
31. Tozzini V. Coarse-grained models for proteins. Curr Opin Struct Biol 2005;15:144–150.
32. Chng CP, Yang LW. Coarse-grained models reveal functional dynamics-II. Molecular dynamics simulation at the coarse-grained level—theories and biological applications. Bioinform Biol Insights. 2008;2:171–185.
33. Ueda Y, Taketomi H, Go N. Studies on protein folding, unfolding, and fluctuations by computer-simulation. 2. 3-dimensional lattice model of lysozyme. Biopolymers 1978;17:1531–1548.
34. Koga N, Takada S. Folding-based molecular simulations reveal mechanisms of the rotary motor F1-ATPase. Proc Natl Acad Sci USA 2006;103:5367–5372.
35. Hinsen K. Analysis of domain motions by approximate normal mode calculations. Proteins 1998;33:417–429.
36. Atilgan AR, Durell SR, Jernigan RL, Demirel MC, Keskin O, Bahar I. Anisotropy of fluctuation dynamics of proteins with an elastic network model. Biophys J 2001;80:505–515.
37. Tama F, Sanejouand YH. Conformational change of proteins arising from normal mode calculations. Protein Eng 2001;14:1–6.
38. Tirion MM. Large amplitude elastic motions in proteins from a single-parameter, atomic analysis. Phys Rev Lett 1996;77:1905–1908.
39. Krebs WG, Alexandrov V, Wilson CA, Echols N, Yu HY, Gerstein M. Normal mode analysis of macromolecular motions in a database framework: developing mode concentration as a useful classifying statistic. Proteins 2002;48:682–695.
40. Yang L, Song G, Jernigan RL. How well can we understand large-scale protein motions using normal modes of elastic network models? Biophys J 2007;93:920–929.
41. Ma J. Usefulness and limitations of normal mode analysis in modeling dynamics of biomolecular complexes. Structure 2005;13:373–380.
42. Bahar I, Rader AJ. Coarse-grained normal mode analysis in structural biology. Curr Opin Struct Biol 2005;15:586–592.
43. Tama F, Brooks CL. Symmetry, form, and shape: guiding principles for robustness in macromolecular machines. Annu Rev Biophys Biomol Struct 2006;35:115–133.
44. Miyashita O, Onuchic JN, Wolynes PG. Nonlinear elasticity, proteinquakes, and the energy landscapes of functional transitions in proteins. Proc Natl Acad Sci USA 2003;100:12570–12575.
45. Maragakis P, Karplus M. Large amplitude conformational change in proteins explored with a plastic network model: adenylate kinase. J Mol Biol 2005;352:807–822.
46. Zheng WJ, Brooks BR, Hummer G. Protein conformational transitions explored by mixed elastic network models. Proteins 2007;69:43–57.
47. Franklin J, Koehl P, Doniach S, Delarue M. MinActionPath: maximum likelihood trajectory for large-scale structural transitions in a coarse-grained locally harmonic energy landscape. Nucleic Acids Res 2007;35:W477–W482.
48. Chu JW, Voth GA. Coarse-grained free energy functions for studying protein conformational changes: a double-well network model. Biophys J. 2007;93:3860–3871.
49. Zhu FQ, Hummer G. Gating transition of pentameric ligand-gated ion channels. Biophys J 2009;97:2456–2463.
50. Weiss DR, Levitt M. Can morphing methods predict intermediate structures? J Mol Biol 2009;385:665–674.
51. Yang LW, Chng CP. Coarse-grained models reveal functional dynamics-I. Elastic network models—theories, comparisons and perspectives. Bioinform Biol Insights 2008;2:25–45.
52. Best RB, Chen YG, Hummer G. Slow protein conformational dynamics from multiple experimental structures: the helix/sheet transition of arc repressor. Structure 2005;13:1755–1763.
53. Chen YQ, Davis TA, Hager WW, Rajamanickam S. Algorithm 887: CHOLMOD, supernodal sparse cholesky factorization and update/downdate. Acm Trans Math Software 2008;35:22.
54. Zheng W. Multiscale modeling of structural dynamics underlying force generation and product release in actomyosin complex. Proteins 2010;78:638–660.
55. Sellers JR. Myosins: a diverse superfamily. Biochim Biophys Acta 2000;1496:3–22.
56. Geeves MA, Holmes KC. Structural mechanism of muscle contraction. Annu Rev Biochem 1999;68:687–728.
57. Spudich JA. The myosin swinging cross-bridge model. Nat Rev Mol Cell Biol 2001;2:387–392.
58. Tyska MJ, Warshaw DM. The myosin power stroke. Cell Motil Cytoskeleton 2002;51:1–15.

59. Lymn RW, Taylor EW. Mechanism of adenosine triphosphate hydrolysis by actomyosin. Biochemistry 1971;10:4617–4624.
60. Taylor EW. Mechanism of actomyosin ATPase and the problem of muscle contraction. CRC Crit Rev Biochem 1979;6:103–164.
61. De La Cruz EM, Ostap EM. Relating biochemistry and function in the myosin superfamily. Curr Opin Cell Biol 2004;16:61–67.
62. Houdusse A, Szent-Gyorgyi AG, Cohen C. Three conformational states of scallop myosin S1. Proc Natl Acad Sci USA 2000;97: 11238–11243.
63. Reubold TF, Eschenburg S, Becker A, Kull FJ, Manstein DJ. A structural model for actin-induced nucleotide release in myosin. Nat Struct Biol 2003;10:826–830.
64. Coureux PD, Wells AL, Menetry J, Yengo CM, Morris CA, Sweeney HL, Houdusse A. A structural state of the myosin V motor without bound nucleotide. Nature 2003;425:419–423.
65. Coureux PD, Sweeney HL, Houdusse A. Three myosin V structures delineate essential features of chemo-mechanical transduction. EMBO J 2004;23:4527–4537.
66. Yang YT, Gourinath S, Kovacs M, Nyitray L, Reutzel R, Himmel DM, O'Neall-Hennessey E, Reshetnikova L, Szent-Gyorgyi AG, Brown JH, Cohen C. Rigor-like structures from muscle myosins reveal key mechanical elements in the transduction pathways of this allosteric motor. Structure 2007;15:553–564.
67. Zheng WJ, Brooks B. Identification of dynamical correlations within the myosin motor domain by the normal mode analysis of an elastic network model. J Mol Biol 2005;346:745–759.
68. Zheng W, Brooks BR, Thirumalai D. Low-frequency normal modes that describe allosteric transitions in biological nanomachines are robust to sequence variations. Proc Natl Acad Sci USA 2006;103:7664–7669.
69. Zheng WJ, Thirumalai D. Coupling between normal modes drives protein conformational dynamics: illustrations using allosteric transitions in myosin II. Biophys J 2009;96:2128–2137.
70. Cecchini M, Houdusse A, Karplus M. Allosteric communication in myosin v: from small conformational changes to large directed movements. Plos Comput Biol 2008;4:e1000129.
71. Fischer S, Windshugel B, Horak D, Holmes KC, Smith JC. Structural mechanism of the recovery stroke in the myosin molecular motor. Proc Natl Acad Sci USA 2005;102:6873–6878.
72. Yu H, Ma L, Yang Y, Cui Q. Mechanochemical coupling in the myosin motor domain. II. Analysis of critical residues. Plos Comput Biol 2007;3:214–230.
73. Yang Y, Yu H, Cui Q. Extensive conformational transitions are required to turn on ATP hydrolysis in myosin. J Mol Biol 2008; 381:1407–1420.
74. Woo HJ. Exploration of the conformational space of myosin recovery stroke via 75. molecular dynamics. Biophys Chem 2007;125: 127–137.
75. Koppole S, Smith JC, Fischer S. Simulations of the myosin II motor reveal a nucleotide-state sensing element that controls the recovery stroke. J Mol Biol 2006;361:604–616.
76. Koppole S, Smith JC, Fischer S. The structural coupling between ATPase activation and recovery stroke in the myosin II motor. Structure 2007;15:825–837.
77. Mesentean S, Koppole S, Smith JC, Fischer S. The principal motions involved in the coupling mechanism of the recovery stroke of the myosin motor. J Mol Biol 2007;367:591–602.
78. Fiser A, Sali A. ModLoop: automated modeling of loops in protein structures. Bioinformatics 2003;19:2500–2501.
79. Krebs WG, Gerstein M. The morph server: a standardized system for analyzing and visualizing macromolecular motions in a database framework. Nucleic Acids Res 2000;28:1665–1675.
80. Smith DA, Sleep J. Mechanokinetics of rapid tension recovery in muscle: the myosin working stroke is followed by a slower release of phosphate. Biophys J 2004;87:442–456.
81. Takagi Y, Shuman H, Goldman YE. Coupling between phosphate release and force generation in muscle actomyosin. Philosophical Trans R Soc London Series B: Biol Sci 2004;359:1913–1920.
82. Nakamoto RK, Scanlon JAB, Al-Shawi MK. The rotary mechanism of the ATP synthase. Arch Biochem Biophys 2008;476:43–50.
83. Gibbons C, Montgomery MG, Leslie AG, Walker JE. The structure of the central stalk in bovine F(1)-ATPase at 2.4 A resolution. Nat Struct Biol 2000;7:1055–1061.
84. Walker JE, Saraste M, Runswick MJ, Gay NJ. Distantly related sequences in the alpha-subunits and beta-subunits of atp synthase, myosin, kinases and other Atp-requiring enzymes and a common nucleotide binding fold. EMBO J 1982;1:945–951.
85. Nadanaciva S, Weber J, Wilke-Mounts S, Senior AE. Importance of F-1-ATPase residue alpha-Arg-376 for catalytic transition state stabilization. Biochemistry 1999;38:15493–15499.
86. Cross RL, Grubmeyer C, Penefsky HS. Mechanism of Atp hydrolysis by beef-heart mitochondrial ATpase—rate enhancements resulting from cooperative interactions between multiple catalytic sites. J Biol Chem 1982;257:2101–2105.
87. Gresser MJ, Myers JA, Boyer PD. Catalytic site cooperativity of beef heart mitochondrial F1 adenosine triphosphatase. Correlations of initial velocity, bound intermediate, and oxygen exchange measurements with an alternating three-site model. J Biol Chem 1982;257:12030–12038.
88. Grubmeyer C, Cross RL, Penefsky HS. Mechanism of Atp hydrolysis by beef-heart mitochondrial ATPase—rate constants for elementary steps in catalysis at a single site. J Biol Chem 1982;257:2092–2100.
89. Kayalar C, Rosing J, Boyer PD. Alternating site sequence for oxidative-phosphorylation suggested by measurement of substrate binding patterns and exchange-reaction inhibitions. J Biol Chem 1977;252:2486–2491.
90. Boyer PD. The binding change mechanism for Atp synthase—some probabilities and possibilities. Biochim Biophys Acta 1993;1140:215–250.
91. Yasuda R, Noji H, Kinosita K, Yoshida M. F-1-ATPase is a highly efficient molecular motor that rotates with discrete 120 degrees steps. Cell 1998;93:1117–1124.
92. Adachi K, Yasuda R, Noji H, Itoh H, Harada Y, Yoshida M, Kinosita K. Stepping rotation of F-1-ATPase visualized through angle-resolved single-fluorophore imaging. Proc Natl Acad Sci USA 2000;97:7243–7247.
93. Yasuda R, Noji H, Yoshida M, Kinosita K, Itoh H. Resolution of distinct rotational substeps by submillisecond kinetic analysis of F-1-ATPase. Nature 2001;410:898–904.
94. Nishizaka T, Oiwa K, Noji H, Kimura S, Muneyuki E, Yoshida M, Kinosita K, Jr. Chemomechanical coupling in F1-ATPase revealed by simultaneous observation of nucleotide kinetics and rotation. Nat Struct Mol Biol 2004;11:142–148.
95. Ariga T, Muneyuki E, Yoshida M. F1-ATPase rotates by an asymmetric, sequential mechanism using all three catalytic subunits. Nat Struct Mol Biol 2007;14:984–984.
96. Wang HY, Oster G. Energy transduction in the F-1 motor of ATP synthase. Nature 1998;396:279–282.
97. Sun SX, Wang HY, Oster G. Asymmetry in the F-1-ATPase and its implications for the rotational cycle. Biophys J 2004;86:1373–1384.
98. Yang W, Gao YQ, Cui Q, Ma J, Karplus M. The missing link between thermodynamics and structure in F1-ATPase. Proc Natl Acad Sci USA 2003;100:874–879.
99. Gao YQ, Yang W, Marcus RA, Karplus M. A model for the cooperative free energy transduction and kinetics of ATP hydrolysis by F-1-ATPase. Proc Natl Acad Sci USA 2003;100:11339–11344.
100. Dittrich M, Hayashi S, Schulten K. On the mechanism of ATP hydrolysis in F-1-ATPase. Biophys J 2003;85:2253–2266.
101. Dittrich M, Hayashi S, Schulten K. ATP hydrolysis in the betaTP and betaDP catalytic sites of F1-ATPase. Biophys J 2004;87:2954–2967.
102. Bockmann RA, Gruhmuller H. Nanoseconds molecular dynamics simulation of primary mechanical energy transfer steps in F1-ATP synthase. Abst Paper Am Chem Soc 2003;225:U519–U520.

103. Bockmann RA, Grubmuller H. Conformational dynamics of the F-1-ATPase beta-subunit: a molecular dynamics study. Biophys J 2003;85:1482–1491.
104. Ma JP, Flynn TC, Cui Q, Leslie AGW, Walker JE, Karplus M. A dynamic analysis of the rotation mechanism for conformational change in F-1-ATPase. Structure 2002;10:921–931.
105. Antes I, Chandler D, Wang HY, Oster G. The unbinding of ATP from F-1-ATPase. Biophys J 2003;85:695–706.
106. Koga N, Takada S. Folding-based molecular simulations reveal mechanisms of the rotary motor F1-ATPase. Proc Natl Acad Sci USA 2006;103:5367–5372.
107. Pu J, Karplus M. How subunit coupling produces the gamma-subunit rotary motion in F1-ATPase. Proc Natl Acad Sci USA 2008;105:1192–1197.
108. Zheng W. Normal-mode-based modeling of allosteric couplings that underlie cyclic conformational transition in F(1) ATPase. Proteins 2009;76:747–762.
109. Oster G, Wang HY. Why is the mechanical efficiency of F-1-ATPase so high? J Bioenerg Biomembr 2000;32:459–469.
110. Kinosita K, Jr., Adachi K, Itoh H. Rotation of F1-ATPase: how an ATP-driven molecular machine may work. Annu Rev Biophys Biomol Struct 2004;33:245–268.
111. Zheng W, Liao JC, Brooks BR, Doniach S. Toward the mechanism of dynamical couplings and translocation in hepatitis C virus NS3 helicase using elastic network model. Proteins 2007;67:886–896.
112. Menz RI, Walker JE, Leslie AG. Structure of bovine mitochondrial F(1)-ATPase with nucleotide bound to all three catalytic sites: implications for the mechanism of rotary catalysis. Cell 2001;106:331–341.
113. Weber J, Senior AE. Catalytic mechanism of F-1-ATPase. Biochimica Et Biophysica Acta-Bioenergetics 1997;1319:19–58.
114. Xu ZH, Horwich AL, Sigler PB. The crystal structure of the asymmetric GroEL-GroES-(ADP)(7) chaperonin complex. Nature 1997;388:741–750.
115. Thirumalai D, Lorimer GH. Chaperonin-mediated protein folding. Annu Rev Biophys Biomol Struct 2001;30:245–269.
116. Ranson NA, Farr GW, Roseman AM, Gowen B, Fenton WA, Horwich AL, Saibil HR. ATP-bound states of GroEL captured by cryo-electron microscopy. Cell 2001;107:869–879.
117. Ma JP, Karplus M. The allosteric mechanism of the chaperonin GroEL: a dynamic analysis. Proc Natl Acad Sci USA 1998;95:8502–8507.
118. Ma JP, Sigler PB, Xu ZH, Karplus M. A dynamic model for the allosteric mechanism of GroEL. J Mol Biol 2000;302:303–313.
119. Keskin O, Bahar I, Flatow D, Covell DG, Jernigan RL. Molecular mechanisms of chaperonin GroEL-GroES function. Biochemistry 2002;41:491–501.
120. Zheng W, Brooks BR, Thirumalai D. Allosteric transitions in the chaperonin GroEL are captured by a dominant normal mode that is most robust to sequence variations. Biophys J 2007;93:2289–2299.
121. Hyeon C, Lorimer GH, Thirumalai D. Dynamics of allosteric transitions in GroEL. Proc Natl Acad Sci USA 2006;103:18939–18944.
122. Stan G, Thirumalai D, Lorimer GH, Brooks BR. Annealing function of GroEL: structural and bioinformatic analysis. Biophys Chem 2003;100:453–467.
123. Stan G, Brooks BR, Thirumalai D. Probing the "annealing" mechanism of GroEL minichaperone using molecular dynamics simulations. J Mol Biol 2005;350:817–829.
124. Stan G, Brooks BR, Lorimer GH, Thirumalai D. Residues in substrate proteins that interact with GroEL in the capture process are buried in the native state. Proc Natl Acad Sci USA 2006;103:4433–4438.
125. Stan G, Lorimer GH, Thirumalai D, Brooks BR. Coupling between allosteric transitions in GroEL and assisted folding of a substrate protein. Proc Natl Acad Sci USA 2007;104:8803–8808.
126. Tehver R, Chen J, Thirumalai D. Allostery wiring diagrams in the transitions that drive the GroEL reaction Cycle. J Mol Biol 2009;387:390–406.
127. Chennubhotla C, Bahar I. Markov propagation of allosteric effects in biomolecular systems: application to GroEL-GroES. Mol Syst Biol 2006;2:36.
128. Chennubhotla C, Yang Z, Bahar I. Coupling between global dynamics and signal transduction pathways: a mechanism of allostery for chaperonin GroEL. Mol Biosyst 2008;4:287–292.
129. Yang Z, Majek P, Bahar I. Allosteric transitions of supramolecular systems explored by network models: application to chaperonin GroEL. Plos Comput Biol 2009;5:e1000360.
130. Coluzza I, De Simone A, Fraternali F, Frenkel D. Multi-scale simulations provide supporting evidence for the hypothesis of intramolecular protein translocation in GroEL/GroES complexes. Plos Comput Biol 2008;4:e1000006.
131. Sliozberg Y, Abrams CF. Spontaneous conformational changes in the *E. coli* GroEL subunit from all-atom molecular dynamics Simulations. Biophys J 2007;93:1906–1916.
132. van der Vaart A, Ma JP, Karplus M. The unfolding action of GroEL on a protein substrate. Biophys J 2004;87:562–573.
133. de Groot BL, Vriend G, Berendsen HJC. Conformational changes in the chaperonin GroEL: new insights into the allosteric mechanism. J Mol Biol 1999;286:1241–1249.
134. Zheng WJ, Brooks BR. Probing the local dynamics of nucleotide-binding pocket coupled to the global dynamics: myosin versus kinesin. Biophys J 2005;89:167–178.
135. Noji H, Yasuda R, Yoshida M, Kinosita K. Direct observation of the rotation of F-1-ATPase. Nature 1997;386:299–302.